

## Domain-size dependence of piezoelectric properties of ferroelectrics

Rajeev Ahluwalia,<sup>1</sup> Turab Lookman,<sup>1</sup> Avadh Saxena,<sup>1</sup> and Wenwu Cao<sup>2</sup>

<sup>1</sup>Theoretical Division, Los Alamos National Laboratory, Los Alamos, New Mexico 87545, USA

<sup>2</sup>Materials Research Institute and Department of Mathematics, Pennsylvania State University, University Park, Pennsylvania 16802, USA

(Received 14 October 2004; revised manuscript received 11 February 2005; published 13 July 2005)

The domain-size dependence of the piezoelectric properties of ferroelectrics is investigated using a continuum Ginzburg-Landau model that incorporates long-range elastic and electrostatic interactions. Microstructures with the desired domain sizes are created by quenching from the paraelectric phase by biasing the initial conditions. Three different two-dimensional microstructures with different sizes of the 90° domains are simulated. An electric field is applied along the polar as well as nonpolar directions and the piezoelectric response is simulated as a function of domain size for both cases. The simulations show that the piezoelectric coefficients are enhanced by reducing the domain size, consistent with recent experimental results of Wada and Tsurumi [Br. Ceram. Trans. **103**, 93 (2004)] on domain-engineered BaTiO<sub>3</sub> single crystals.

DOI: [10.1103/PhysRevB.72.014112](https://doi.org/10.1103/PhysRevB.72.014112)

PACS number(s): 77.65.Ly, 74.20.De, 77.80.-e

### I. INTRODUCTION

Ferroelectrics are excellent piezoelectric materials that can convert electrical energy into mechanical energy and vice versa.<sup>1</sup> This electromechanical property arises due to the coupling of spontaneous polarization with lattice strain. Many devices such as ultrasonic transducers and piezoelectric actuators make use of this property.<sup>2</sup> Recently, there has been considerable interest in this field due to the observation of a giant piezoelectric response if the applied field is along a nonpolar direction.<sup>3,4</sup> It is believed that this “superpiezoelectric” response is due to the symmetry change caused by a rotation of the polarization towards the direction of the applied field.<sup>5</sup> Domain configurations produced by the field applied in the nonpolar direction are termed *engineered domains*. There are also a large number of domain walls between the degenerate variants which affect the piezoelectric property. In a recent paper, Wada and Tsurumi<sup>6</sup> studied the dependence of the piezoelectric properties of domain-engineered BaTiO<sub>3</sub> single crystals as a function of domain size. Engineered domain configurations with a range of domain sizes were synthesized. The study revealed that piezoelectricity is enhanced for domain-engineered crystals with small domain sizes (or high domain wall density). Thus, domain walls influence the piezoelectric properties and it is important to compute the contribution of the domain walls to the piezoelectric response.

The electromechanical properties of ferroelectrics have been studied theoretically using first-principles calculations.<sup>5,7,8</sup> A continuum Landau theory describing a single domain or homogeneous state has been used to study the electromechanical properties of BaTiO<sub>3</sub> as a function of temperature and electric field direction.<sup>9</sup> Although such calculations provide valuable insights into the physics of the polarization-strain coupling, they do not describe inhomogeneities due to domains and domain walls. Recently, we studied the piezoelectric properties of domain-engineered two-dimensional (2D) ferroelectrics using the time-dependent Ginzburg Landau (TDGL) theory.<sup>10</sup> The conclusion from our simulations showed the importance of the role played by the

domain walls in nucleating an electric-field-induced structural transition if an electric field is applied along a nonpolar direction. We showed that the field-induced transition occurred at lower electric fields for a multidomain state, compared to an analogous situation for a single-domain state. To understand the recent experimental results of Wada and Tsurumi<sup>6</sup> that show piezoelectric enhancement at small domain sizes, we extend in this paper the TDGL model to investigate the dependence of piezoelectricity on the size of the 90° domains in the system and the domain wall density. Unlike Ref. 10 where the domain microstructure was obtained by quenching from the paraelectric phase with random initial conditions, here we create domain structures with the desired sizes by appropriately biasing the initial conditions. This procedure allows us to obtain domain microstructures with a range of domain sizes. The size dependence is studied for the case with the electric field along a polar axis as well as that with the field along a nonpolar direction.

The paper is organized as follows. In Sec. II, we describe the model in detail. Section III describes our simulations for the case of the electric field applied along a polar axis. In Sec. IV, we discuss the case in which the electric field is applied along a nonpolar direction. We conclude in Sec. V with a summary and discussion.

### II. MODEL

The calculations are based on a time-dependent Ginzburg-Landau model<sup>11–13</sup> with long-range elastic and electrostatic effects. We restrict ourselves to a 2D ferroelectric transition to illustrate the basic principles and use parameters from a model for BaTiO<sub>3</sub> in our calculation.<sup>9</sup> The free-energy functional for a 2D ferroelectric system is written as  $F = F_l + F_{em} + F_{es}$ . Here  $F_l$  is the local free energy<sup>9</sup> that describes the ferroelectric transformation and is given by

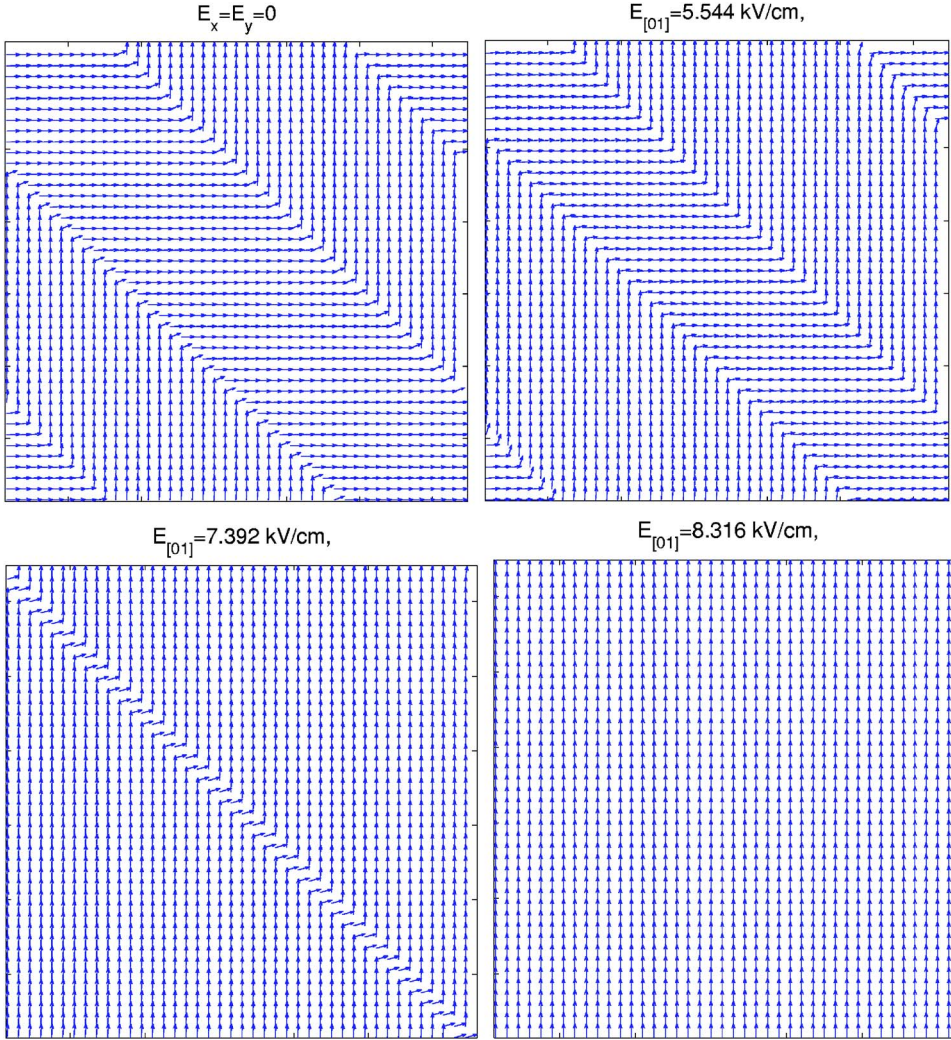


FIG. 1. (Color online) Evolution of domains for an electric field applied along the [01] direction to the multidomain state with domain size  $L_0 \sim 22.6$  nm. The corresponding electric field levels are indicated at the top of each snapshot.

$$F_l = \int d\vec{r} \left\{ \alpha_1 (P_x^2 + P_y^2) + \alpha_{11} (P_x^4 + P_y^4) + \alpha_{12} P_x^2 P_y^2 \right. \\
 + \alpha_{111} (P_x^6 + P_y^6) + \alpha_{112} (P_x^2 P_y^4 + P_x^4 P_y^2) - E_x P_x - E_y P_y \\
 \left. + \frac{g_1}{2} (P_{x,x}^2 + P_{y,y}^2) + \frac{g_2}{2} (P_{x,y}^2 + P_{y,x}^2) + g_3 P_{x,x} P_{y,y} \right\}, \quad (1)$$

where  $P_x$  and  $P_y$  are the polarization components. The free-energy coefficients  $\alpha_1, \alpha_{11}, \dots, \alpha_{112}$  determine the ferroelectric phase and the gradient coefficients  $g_1, g_2,$  and  $g_3$  are a measure of domain wall energies.  $E_x$  and  $E_y$  are the components of an external electric field. Elastic properties are studied by using the strains  $\eta_1 = \eta_{xx} + \eta_{yy}$ ,  $\eta_2 = \eta_{xx} - \eta_{yy}$ , and  $\eta_3 = \eta_{xy}$ , where  $\eta_{ij}$  is the linearized strain tensor defined as  $\eta_{ij} = (u_{i,j} + u_{j,i})/2$  ( $i, j = x, y$ ),  $u_i$  being the components of the displacement vector. The electromechanical coupling is described in terms of these strain variables with the free energy

$$F_{em} = \lambda \int d\vec{r} \left[ \{ \eta_1 - Q_1 (P_x^2 + P_y^2) \}^2 + \{ \eta_2 - Q_2 (P_x^2 - P_y^2) \}^2 \right. \\
 \left. + \{ \eta_3 - Q_3 P_x P_y \}^2 \right]. \quad (2)$$

Here  $Q_1, Q_2,$  and  $Q_3$  are obtained from the electrostrictive constants of the material with  $Q_1 = Q_{11} + Q_{12}$ ,  $Q_2 = Q_{11} - Q_{12}$ , and  $Q_3 = Q_{44}$  (electrostrictive constants describe coupling between strains and polarization—that is,  $\eta_{xx} = Q_{11} P_x^2 + Q_{12} P_y^2$ ,  $\eta_{yy} = Q_{11} P_y^2 + Q_{12} P_x^2$ , and  $\eta_{xy} = Q_{44} P_x P_y$ ). Notice that the free energy  $F_{em}$  vanishes for a homogeneous state since the homogeneous strains in equilibrium are given by  $\eta_1^e = Q_1 (P_x^2 + P_y^2)$ ,  $\eta_2^e = Q_2 (P_x^2 - P_y^2)$ , and  $\eta_3^e = Q_3 P_x P_y$ . The polarizations  $P_x$  and  $P_y$  for the homogeneous states are calculated by minimizing the homogeneous part of the free energy  $F_l$  in Eq. (1). For an inhomogeneous state, the strains  $\eta_1, \eta_2,$  and  $\eta_3$  are related to each other by the elastic compatibility constraint<sup>14</sup>

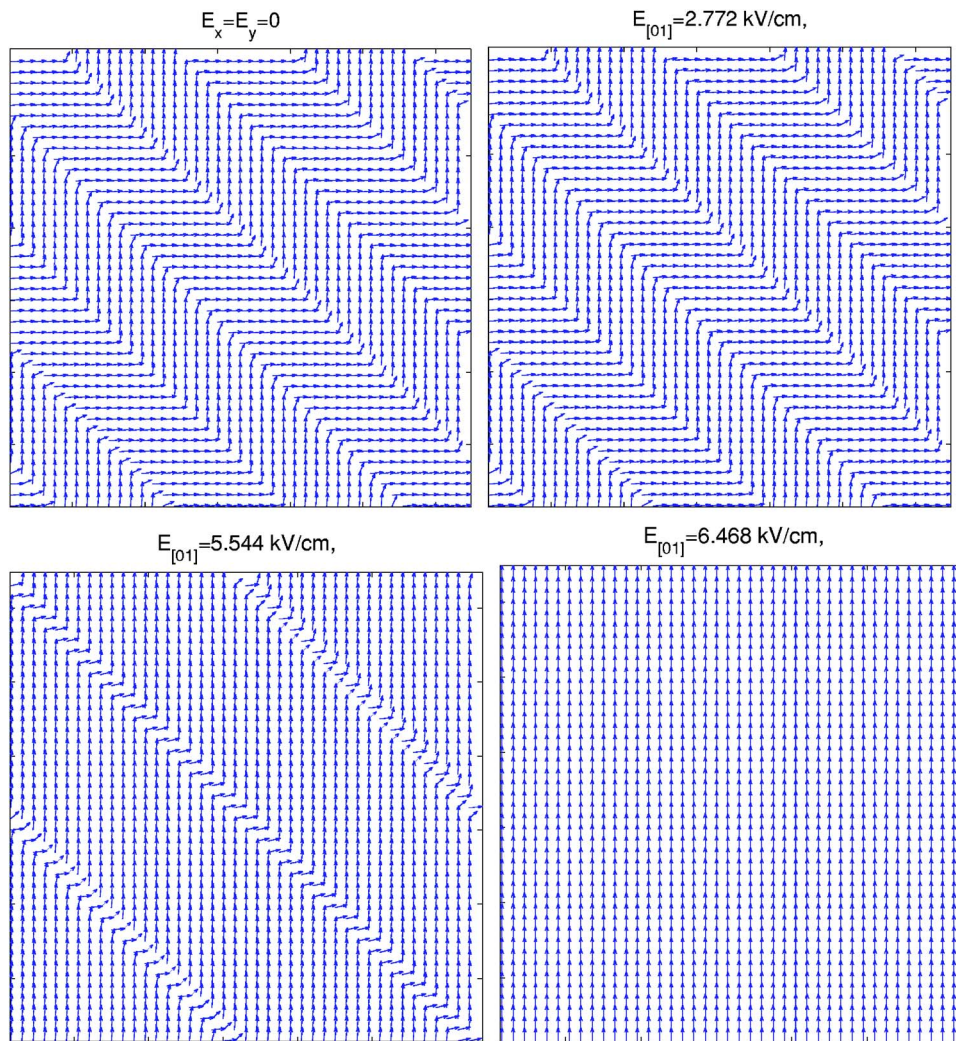


FIG. 2. (Color online) Evolution of domains for an electric field applied along the [01] direction to the multidomain state with domain size  $L_0 \sim 11.3$  nm. The corresponding electric field levels are indicated at the top of each snapshot.

$$\nabla^2 \eta_1 - \left( \frac{\partial^2}{\partial x^2} - \frac{\partial^2}{\partial y^2} \right) \eta_2 - \frac{\partial^2}{\partial x \partial y} \eta_3 = 0. \quad (3)$$

Using this relation, the strain  $\eta_1$  can be eliminated from  $F_{em}$ , resulting in a nonlocal interaction between the strains involving  $\eta_2$  and  $\eta_3$ . Using the equilibrium strains defined by  $\eta_2^e$  and  $\eta_3^e$ , the electromechanical free energy for an inhomogeneous state can be written as

$$F_{em}^{inh} = \lambda \int d\vec{k} [C_2(\vec{k})\Gamma_2(\vec{k}) + C_3(\vec{k})\Gamma_3(\vec{k}) - \Gamma_1(\vec{k})]^2. \quad (4)$$

The constant  $\lambda$  is the strength of this nonlocal interaction and hence it influences the underlying microstructure. Note that the above integral vanishes for the homogeneous  $\vec{k}=0$  modes since, in the present model, the free energy for the homogeneous state is purely given by the homogeneous part of  $F_l$ . The strains for the inhomogeneous states are also given by  $\eta_1^e = Q_1(P_x^2 + P_y^2)$ ,  $\eta_2^e = Q_2(P_x^2 - P_y^2)$ , and  $\eta_3^e = Q_3 P_x P_y$ , but the local polarizations  $P_x$  and  $P_y$  for this case are calculated by minimizing the full inhomogeneous free energy  $F = F_l + F_{em}^{inh}$ .

The quantities  $\Gamma_1(\vec{k})$ ,  $\Gamma_2(\vec{k})$ , and  $\Gamma_3(\vec{k})$  are respectively the Fourier transforms of  $Q_1(P_x^2 + P_y^2)$ ,  $Q_2(P_x^2 - P_y^2)$ , and  $Q_3 P_x P_y$ ;  $C_2 = (k_x^2 - k_y^2)/(k_x^2 + k_y^2)$  and  $C_3 = k_x k_y / (k_x^2 + k_y^2)$  are the orientation-dependent kernels.

The electrostatic contribution to the free energy is calculated by considering the depolarization energy<sup>15</sup>

$$F_{es} = -\mu \int d\vec{r} \{ \vec{E}_d \cdot \vec{P} + \epsilon_0 (\vec{E}_d \cdot \vec{E}_d / 2) \}, \quad (5)$$

where  $\vec{E}_d$  is the internal depolarization field due to the dipoles and  $\mu$  is the strength of this interaction. The field  $\vec{E}_d$  can be calculated from an underlying potential using  $\vec{E}_d = -\vec{\nabla} \phi$ . If we assume that there is no free charge in the system, then  $\vec{\nabla} \cdot \vec{D} = 0$ , where  $\vec{D}$  is the electric displacement vector defined by  $\vec{D} = \epsilon_0 \vec{E}_d + \vec{P}$ . This equation gives rise to the constraint  $-\epsilon_0 \nabla^2 \phi + \vec{\nabla} \cdot \vec{P} = 0$ . The potential  $\phi$  is eliminated from the free energy  $F_{es}$  using the above constraint to express  $F_{es}$  in Fourier space as

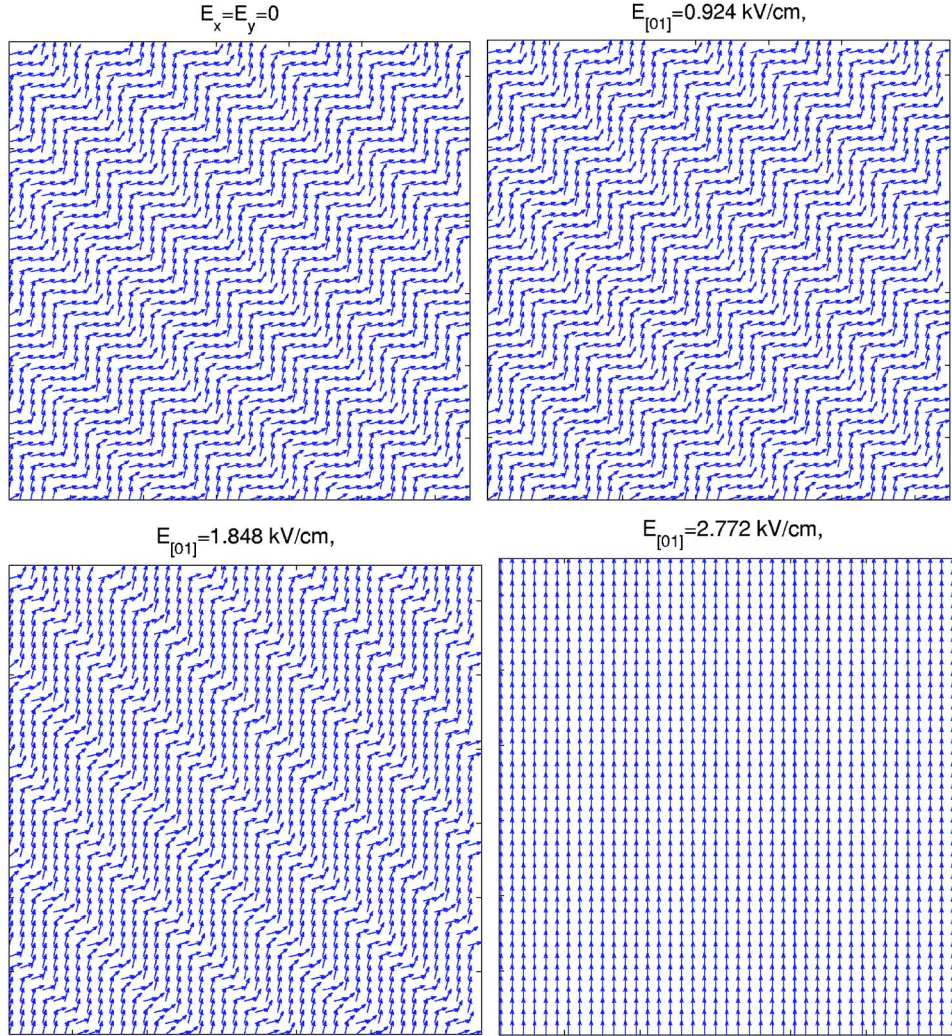


FIG. 3. (Color online) Evolution of domains for an electric field applied along the [01] direction to the multidomain state with domain size  $L_0 \sim 4.5$  nm. The corresponding electric field levels are indicated at the top of each snapshot.

$$F_{es} = \frac{\mu}{2\epsilon_0} \int d\vec{k} [\hat{k}_x P_x(\vec{k}) + \hat{k}_y P_y(\vec{k})]^2. \quad (6)$$

The above integral excludes the homogeneous  $\vec{k}=0$  mode which means that the homogeneous depolarization field due to surface charges has been neglected. The total energy is defined by  $F = F_l + F_{em} + F_{es}$  with two additional constants; i.e.,  $\lambda$  and  $\mu$ , which are essential for the description of multidomain states.

The dynamics of the polarization fields is given by the relaxational time-dependent Ginzburg-Landau equations

$$\frac{\partial P_i}{\partial t} = -\gamma \frac{\delta F}{\delta P_i}, \quad (7)$$

where  $\gamma$  is a dissipation coefficient and  $i=x,y$  represents the polarization components. We first introduce rescaled variables defined with  $u = P_x/P_0$ ,  $v = P_y/P_0$ ,  $\vec{\zeta} = \vec{r}/\delta$ , and  $t^* = \gamma|\alpha_1(T_0)|t$ , where  $T_0$  is a fixed temperature. In this work, we use the parameters<sup>9</sup> for BaTiO<sub>3</sub> for the local

part of the free energy  $F_l$ . The parameters which can be dependent on the temperature  $T$  are  $\alpha_1 = 3.34 \times 10^5 (T - 381) \text{ V m C}^{-1}$ ,  $\alpha_{11} = 4.69 \times 10^6 (T - 393) - 2.02 \times 10^8 \text{ V m}^5 \text{ C}^{-3}$ ,  $\alpha_{111} = -5.52 \times 10^7 (T - 393) + 2.76 \times 10^9 \text{ V m}^9 \text{ C}^{-5}$ ,  $\alpha_{12} = 3.23 \times 10^8 \text{ V m}^5 \text{ C}^{-3}$ , and  $\alpha_{112} = 4.47 \times 10^9 \text{ V m}^9 \text{ C}^{-5}$ . The electrostrictive constants are given as  $Q_{11} = 0.11 \text{ m}^4 \text{ C}^{-2}$ ,  $Q_{12} = -0.045 \text{ m}^4 \text{ C}^{-2}$ , and  $Q_{44} = 0.029 \text{ m}^4 \text{ C}^{-2}$ . To calculate the rescaled quantities, we use  $T_0 = 298 \text{ K}$  and  $P_0 = 0.26 \text{ C m}^{-2}$  and assume that the coefficients  $g_1 = g_2 = g_3 = g$ . The rescaled gradient coefficient is given as  $g' = g / (|\alpha_1(T_0)|\delta^2)$  and we choose  $g' = 2$  in the simulations. For the experimentally quoted value<sup>16</sup>  $g = 2.5 \times 10^{-9} \text{ V m}^3/\text{C}$ , this corresponds to  $\delta = 6.7 \text{ nm}$ . However, this value of  $\delta$  leads to domain wall widths of the simulated domain structures that are larger than the experimentally observed widths of 1–2 nm. To resolve this, we choose  $g = 1.38 \times 10^{-11} \text{ V m}^3/\text{C}$  corresponding to a  $\delta = 0.5 \text{ nm}$ . The values chosen for the long-range parameters are  $\lambda = 0.25|\alpha_1(T_0)|/P_0^2$  and  $\mu = 20\epsilon_0|\alpha_1(T_0)|$ . These parameters do not influence the homogeneous states but can be used to tune the multidomain structures. The

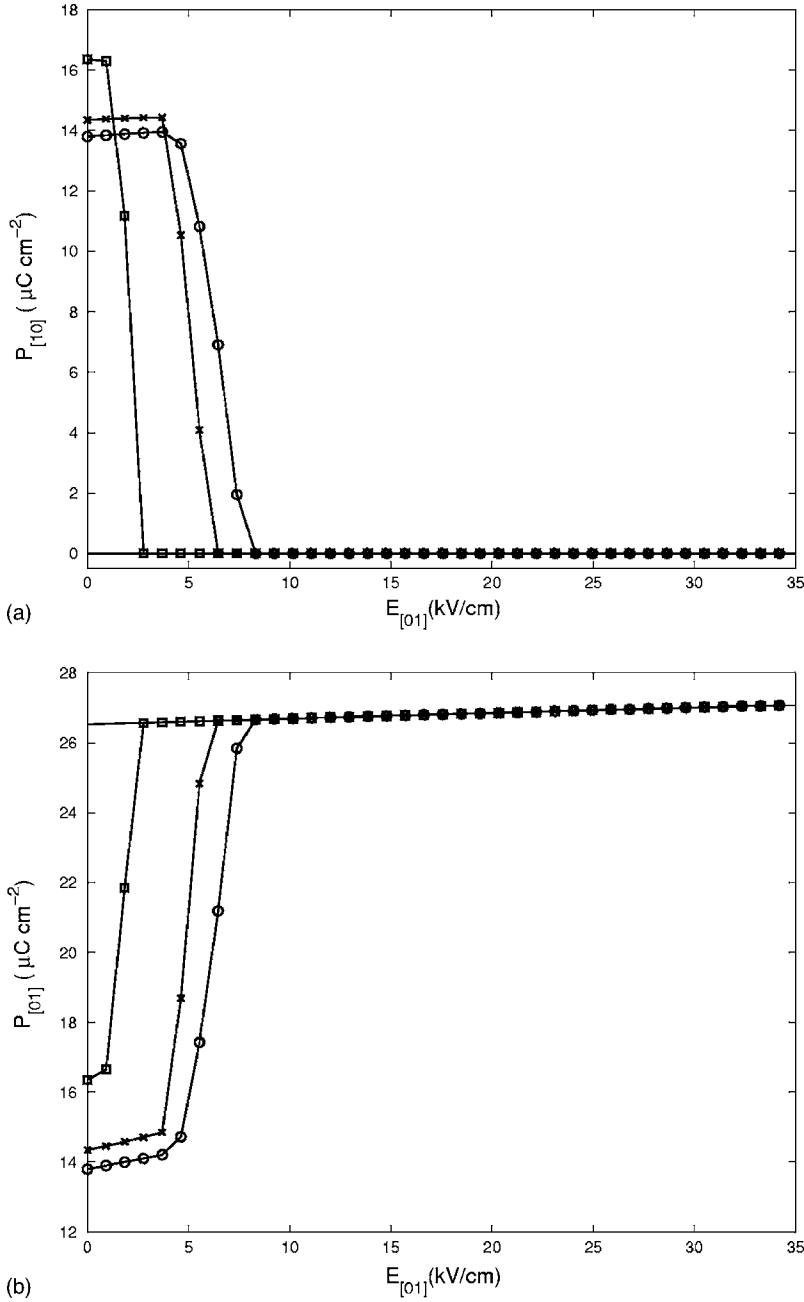


FIG. 4. Evolution of average polarizations  $P_{[10]}$  (a) and  $P_{[01]}$  (b) with the applied field  $E_{[01]}$ . The lines with circles correspond to the multidomain state of Fig. 1 (with domain size  $L_0 \sim 22.6$  nm), lines with crosses correspond to the multidomain state of Fig. 2 (with domain size  $L_0 \sim 11.3$  nm), and lines with squares correspond to the multidomain state of Fig. 3 (with domain size  $L_0 \sim 4.5$  nm). Solid lines correspond to the single-domain state.

present choice of the parameters ensured that multidomain states with all four variants were formed when the domain structure was simulated starting from random initial conditions.<sup>10</sup>

### III. SIMULATIONS

The time-dependent Ginzburg-Landau model with the above rescaled parameters is used to simulate the domain patterns and electromechanical properties. The equations are discretized on a  $128 \times 128$  grid with the Euler scheme using periodic boundary conditions. For the length rescaling factor  $\delta \sim 0.5$  nm, this discretization corresponds to a system of size  $\sim 64$  nm  $\times$  64 nm. We simulate the properties of this 2D

model at  $T=298$  K. At this temperature, the minima of the free energy  $F_l$  define a rectangular ferroelectric phase with the four degenerate states  $(\pm 0.26, 0)$  C m<sup>-2</sup> and  $(0, \pm 0.26)$  C m<sup>-2</sup>. Since we want to study the domain-size dependence of properties, we create domain structures with required domain size instead of letting the domain structure form after a quench from the paraelectric phase. This is achieved by choosing initial conditions based on the following procedure. We consider a function

$$R(x, y) = \cos\left(\frac{N\pi(x+y)}{128\delta}\right). \quad (8)$$

The initial conditions are set up by

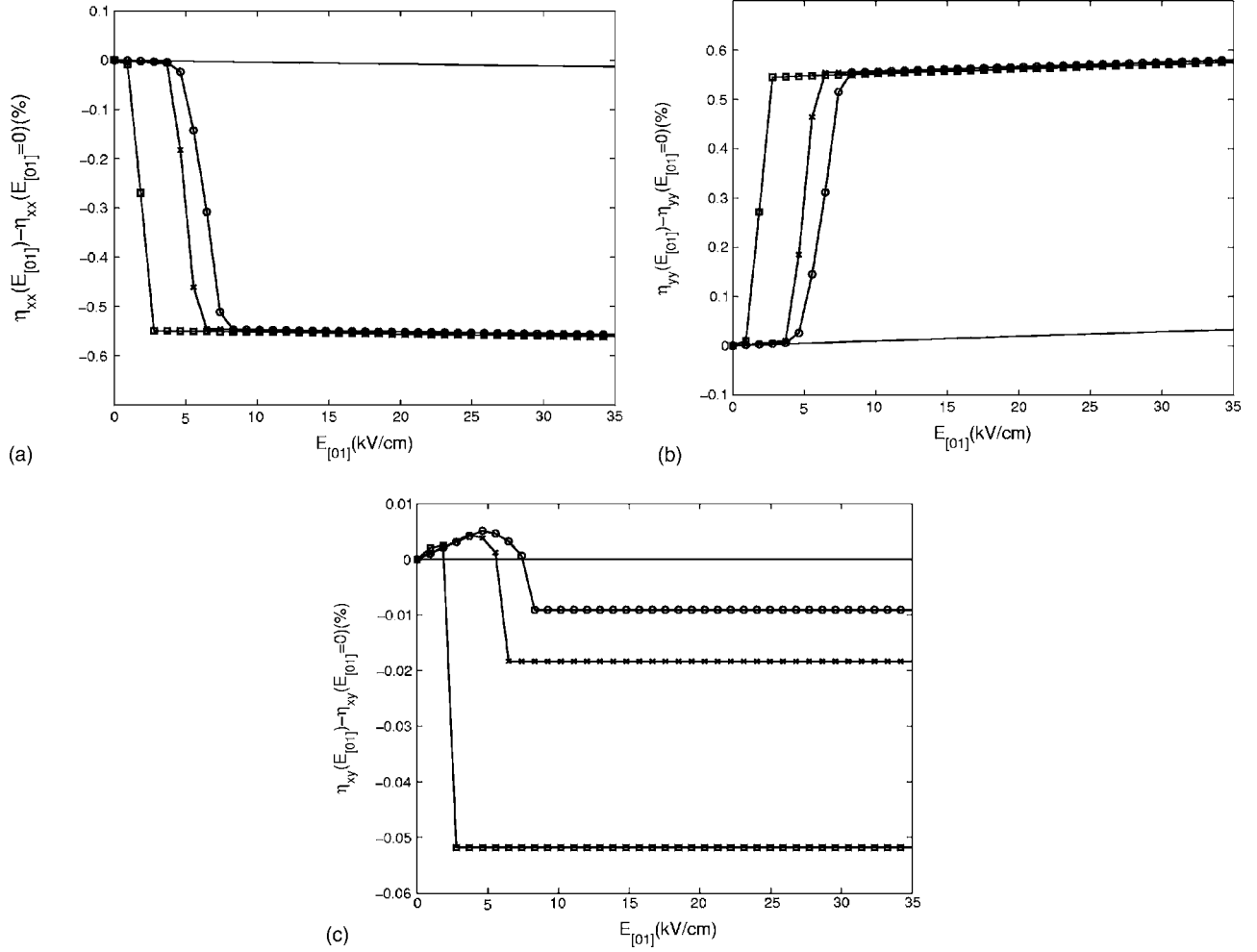


FIG. 5. Evolution of average strains  $\langle \eta_{xx}(E_{[01]}) \rangle - \langle \eta_{xx}(E_{[01]}=0) \rangle$  (a),  $\langle \eta_{yy}(E_{[01]}) \rangle - \langle \eta_{yy}(E_{[01]}=0) \rangle$  (b), and  $\langle \eta_{xy}(E_{[01]}) \rangle - \langle \eta_{xy}(E_{[01]}=0) \rangle$  (c) with the applied field  $E_{[01]}$ . The lines with circles correspond to the multidomain state of Fig. 1 (with domain size  $L_0 \sim 22.6$  nm), lines with crosses correspond to the multidomain state of Fig. 2 (with domain size  $L_0 \sim 11.3$  nm), and lines with squares correspond to the multidomain state of Fig. 3 (with domain size  $L_0 \sim 4.5$  nm). Solid lines correspond to the single-domain state.

$$P_x(x,y) = P_0, \quad P_y(x,y) = 0, \quad R(x,y) > 0,$$

$$P_x(x,y) = 0, \quad P_y(x,y) = P_0, \quad R(x,y) < 0. \quad (9)$$

These initial conditions ensure that multidomain states with head to tail domain walls oriented along  $[11]$  are formed. The above initial conditions also ensure that only two of the four variants with head to tail domain walls are formed in the multidomain. The quantity  $N$  controls the number of domain walls and hence the domain size of the resulting microstructure. We consider the cases  $N=2,4,10$  corresponding respectively to  $90^\circ$  domain patterns with mean domain sizes  $L_0 \sim 22.6, 11.3, 4.5$  nm. The top left snapshots in Figs. 1, 2, and 3 represent the prepared zero-field multidomain states for  $L_0 \sim 22.6, 11.3,$  and  $4.5$  nm, respectively. These were obtained by solving Eq. (7) for a time interval  $t^* = 100$  using the initial conditions given by Eqs. (8) and (9). A close look

at the local dipoles within the domains shows that the polarization vectors are  $(P_0, \Delta)$  and  $(\Delta, P_0)$ , unlike the ideal single crystals which are described by  $(P_0, 0)$  or  $(0, P_0)$ . This means that within the domains, the polarization vectors are slightly rotated compared to the single crystals. As the domain size becomes smaller, the quantity  $\Delta$  increases and the polarization vectors within the domains get increasingly rotated from the ideal  $[10]$  and  $[01]$  directions. This rotation is the largest for the smallest domain size  $L_0 \sim 4.5$  nm [Fig. 3(a)]. This is due to the fact that the domain walls are closely spaced and the width of the diffuse interfaces is comparable to the domain width.

To simulate the effect of an external electric field, the evolution equations are solved with a varying  $\vec{E}$ . We consider two cases: (A) the field applied along the  $[01]$  direction,  $\vec{E} = (0, E_0)$ , corresponding to the polar direction, and (B) the field applied along the  $[11]$  direction,  $\vec{E} = (E_0/\sqrt{2}, E_0/\sqrt{2})$ , corresponding to a nonpolar direction.

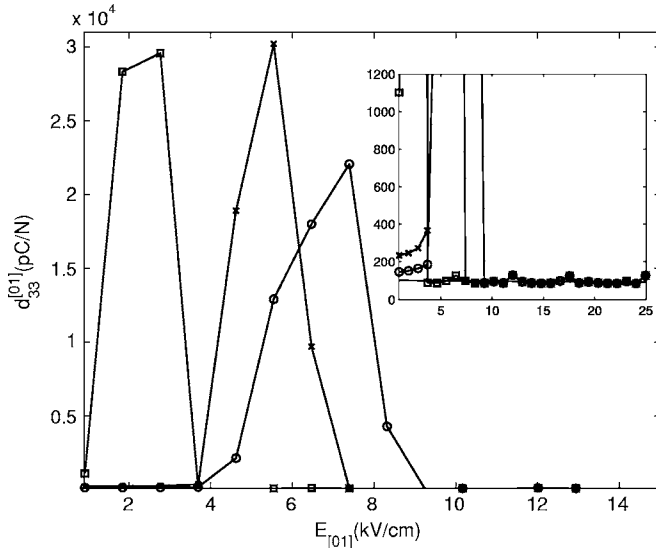


FIG. 6. Variation of  $d_{33}^{[01]}$  (the longitudinal piezoelectric constant along [01]) with  $E_{[01]}$ . The lines with circles correspond to the multidomain state of Fig. 1 (with domain size  $L_0 \sim 22.6$  nm), lines with crosses correspond to the multidomain state of Fig. 2 (with domain size  $L_0 \sim 11.3$  nm), and lines with squares correspond to the multidomain state of Fig. 3 (with domain size  $L_0 \sim 4.5$  nm). Solid lines correspond to the single-domain state. The inset plots the data in the range  $d_{33}^{[01]} < 1200$  pC/N to show the low-field behavior.

### A. Field applied along a polar direction

We first study the traditional scenario when the electric field is applied along one of the polar directions. In the present simulations, we apply the field along the [01] direction which is a polar direction. The field is applied quasistatically—i.e., in fixed increments of  $\Delta E_{[01]} = 0.92$  kV/cm and we let the system relax for  $t^* = 100$  time steps after each change. Since [01] is a polar direction for the parameters used in the present simulations, the state  $(0, 0.26)$  C m<sup>-2</sup> is favored. Figures 1, 2, and 3 show the electric-field-induced domain evolution for domain patterns with mean domain sizes  $L_0 \sim 22.6$ , 11.3, and 4.5 nm, respectively. It can be seen that domains aligned along the [10] direction switch towards the [01] direction, thereby forming a single-domain state for all three cases. A comparison of the evolution in Figs. 1, 2, and 3 shows that a single-domain state is established at smaller electric fields for domain patterns with a larger number of domain walls (or smaller domain sizes). For example, for the smallest domain size  $L_0 \sim 4.5$  nm (Fig. 3), the single domain is established at an electric field  $E_{[01]} \sim 2.5$  kV/cm (this electric field is much smaller than the electric field required to create single-domain states for the domain patterns with  $L_0 \sim 22.6$ , 11.3 nm). Figures 4(a) and 4(b) show the variation of the average polarization with the applied field for the evolution depicted in Figs. 1, 2, and 3. For comparison, we also show the polarization versus electric field response of a single-domain state polarized along [01]—i.e.,  $\vec{P} = (0, 0.26)$  C m<sup>-2</sup>—when an electric field is applied along the [01] direction. Figure 4(a) shows the

evolution of the [10] component of the average polarization,  $P_{[10]}$ . At zero field, for the three cases shown in Figs. 1, 2, and 3,  $P_{[10]}$  has a nonzero value due to coexisting domains and domain walls. Interestingly, this average value increases with decreasing the mean domain size. This increase can be attributed to the rotation of the dipoles within the domains. As discussed earlier, the polarization vectors within the domains are given by  $\vec{P} = (P_0, \Delta)$  or  $\vec{P} = (\Delta, P_0)$ . Since  $\Delta$  increases with decreasing domain size, the average values over the multidomain states also increase as the domain size becomes smaller.

As the electric field is increased along [01],  $P_{[10]}$  decreases to zero for all three cases due to the switching of domains polarized along [10] towards the [01] direction. As discussed earlier,  $P_{[10]}$  reaches zero the fastest for the smallest domain size—i.e.,  $L_0 \sim 4.5$  nm. The single domain  $P_{[10]}$  remains zero, as expected. In Fig. 4(b), we plot the average polarization along the [01] direction,  $P_{[01]}$ , as a function of the applied field  $E_{[01]}$ . Since [01] is a polar direction,  $P_{[01]}$  grows for all the cases. Here, also, the case with the smallest domain size reaches the saturation value the fastest.  $P_{[01]}$  for the single domain varies only slightly with the applied field as there is no domain switching for that case.

To study the electromechanical behavior, we have also computed the variation of the strains with the applied electric field. To evaluate the contribution of the applied electric field to the strain, we subtract off the zero field strain. Figures 5(a), 5(b), and 5(c) show the behavior of average strain components  $\langle \eta_{xx}(E_{[01]}) \rangle - \langle \eta_{xx}(E_{[01]} = 0) \rangle$ ,  $\langle \eta_{yy}(E_{[01]}) \rangle - \langle \eta_{yy}(E_{[01]} = 0) \rangle$ , and  $\langle \eta_{xy}(E_{[01]}) \rangle - \langle \eta_{xy}(E_{[01]} = 0) \rangle$ , respectively. Here  $\eta_{xx} = Q_{11}P_x^2 + Q_{12}P_y^2$ ,  $\eta_{yy} = Q_{11}P_y^2 + Q_{12}P_x^2$ , and  $\eta_{xy} = Q_{44}P_xP_y$ . Since the multidomain states switch to a single-domain state polarized along [01], shrinkage along the transverse [10] direction is observed, as can be seen in Fig. 5(a). The magnitude of this transverse strain is almost the same for all multidomain states, although the field required to establish the single-domain state increases as the domain size is increased. The corresponding single domain undergoes very small shrinkage along the transverse direction as there is no domain switching involved. Figure 5(b) shows the behavior of the longitudinal strain along the direction of the applied field for the three multidomain states as well as the corresponding single-domain states. An expansion along the [01] direction is observed for all the cases. However, the multidomain states generate much larger strains in comparison to the single-domain state. This is due to the 90° domain switching in the multidomain states that results in the extra strain. Figure 5(c) shows the average shear the crystal undergoes during the evolution depicted in Figs. 1, 2, and 3. It is clear that the magnitude of the shear depends on the number of domain walls in the system. This is due to the fact that the domain walls in the unpoled multidomain states are sheared relative to the bulk. Upon applying the electric field, these domain walls disappear, resulting in a net shear strain. Thus the average shear depends on the number of domain walls. The positive shear strain for low fields (“overshoot”) is due to the domain switching process. Since there are no

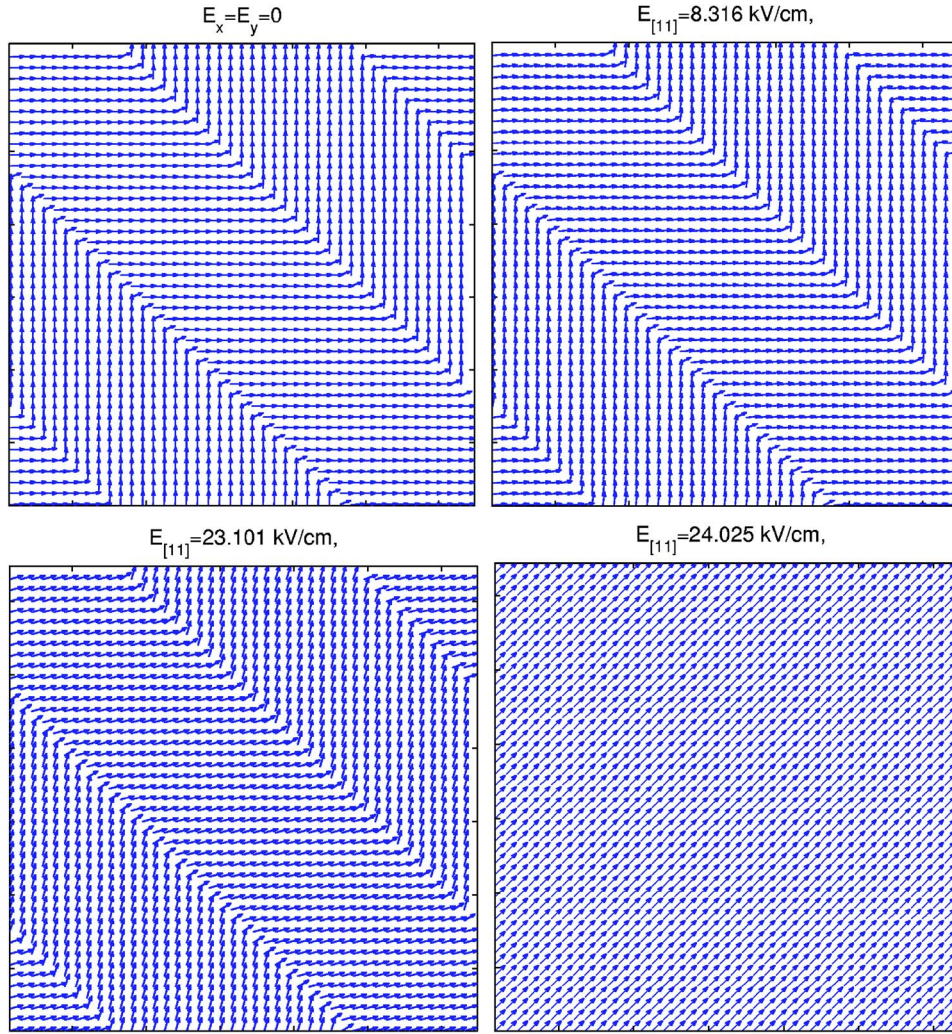


FIG. 7. (Color online) Evolution of domains for an electric field applied along the [11] direction to the multidomain state with domain size  $L_0 \sim 22.6$  nm. The corresponding electric field levels are indicated at the top of each snapshot.

domain walls in the single-domain state, the shear strain is zero for all values of the electric field, as can be observed in Fig. 5(c).

We have also studied the domain-size dependence of the longitudinal piezoelectric coefficient  $d_{33}^{[01]}$ . The piezoelectric coefficients are calculated from the slope of the  $\langle \eta_{yy}(E_{[01]}) \rangle - \langle \eta_{yy}(E_{[01]}=0) \rangle$  vs  $E_{[01]}$  curve in Fig. 5(b). Figure 6 shows the behavior of  $d_{33}^{[01]}$  vs  $E_{[01]}$  for the three multidomain cases along with the analogous single-domain case. The high values observed in the electric field range 0–10 kV/cm are due to the switching of domains. To clearly show the behavior of piezoelectric constants in the low-field regime, we replot the data of this figure in the inset for  $d_{33}^{[01]} < 1200$ . The data in the inset show that the low-field piezoelectric coefficients are enhanced as the domain size is decreased. For example, for the smallest domain size  $L_0 \sim 4.5$  nm,  $d_{33}^{[01]} \sim 1100$  pC/N compared to  $d_{33}^{[01]} \sim 210$  for  $L_0 \sim 22.6$  nm. In the large-field regime ( $E_{[01]} > 10$  kV/cm),  $d_{33}^{[01]}$  is nearly equal for all cases as they all correspond to a poled single-domain state.

### B. Field applied along a nonpolar direction

In this section, we study the case when the configurations depicted in Figs. 1(a), 2(a), and 3(a) are subjected to an electric field along the [11] direction. This situation is a 2D analog of the experiments by Wada and Tsurumi<sup>6</sup> where the electric field was applied along the [111] direction to tetragonal multidomain single crystals of BaTiO<sub>3</sub>.

Here, we apply a quasistatic electric field along the [11] direction. The field is applied in increments of  $\Delta E_{[11]} = 0.92$  kV/cm and the configurations are allowed to relax for  $t^* = 100$  time steps after each change. For this case, application of the field does not immediately result in the creation of a single-domain state along [11]. Instead, the multidomain structure remains stable and the polarization vectors rotate until an electric-field-induced transition to a [11]-polarized rhombic state takes place. This situation is depicted in Figs. 7, 8, and 9 corresponding to the multidomain states with domain sizes  $L_0 \sim 22.6$ , 11.3, and 4.5 nm, respectively. It is observed that the field-induced transition occurs at a lower electric field as the domain size decreases.

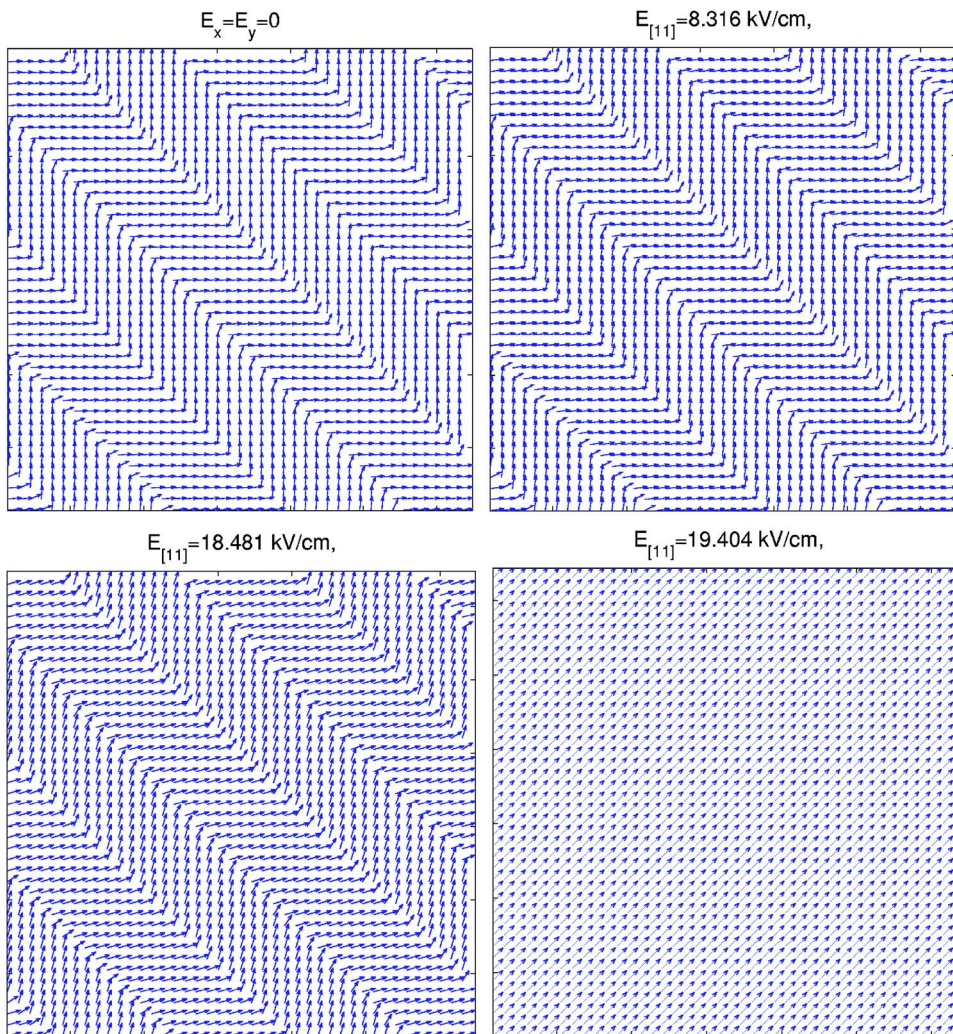


FIG. 8. (Color online) Evolution of domains for an electric field applied along the [11] direction to the multidomain state with domain size  $L_0 \sim 11.3$  nm. The corresponding electric field levels are indicated at the top of each snapshot.

This result corroborates our earlier conclusion that the domain walls help nucleate the field-induced transition.<sup>10</sup> Thus, the larger the number of domain walls, the smaller the field required to induce the transition. For example, for the smallest domain size  $L_0 \sim 4.5$  nm, the transition occurs at  $E_{[11]} \sim 4.6$  kV/cm whereas for the largest domain size  $L_0 \sim 22.6$  nm, the transition occurs at  $E_{[11]} \sim 24$  kV/cm, a very significant change.

The evolution of the components of the average polarization for the situations depicted in Figs. 7, 8, and 9 is plotted in Figs. 10(a) and 10(b). The response of a single-domain state with initial polarization  $(0, 0.26)$  C m<sup>-2</sup> is also shown. The zero-field components  $P_{[10]}$  and  $P_{[01]}$  of the average polarizations for the multidomain states in Figs. 7, 8, and 9 are nonzero due to the coexisting domains of  $(0.26, \Delta)$  C m<sup>-2</sup> and  $(\Delta, 0.26)$  C m<sup>-2</sup>. Since the polarization vectors rotate towards the [11] direction, the evolution of  $P_{[10]}$  and  $P_{[01]}$  is almost identical as both the polarization variants exist in nearly equal proportion. The single domain on the other hand, starts from  $(0, 0.26)$  C m<sup>-2</sup> until it transforms to a rhombic state  $(0.21, 0.21)$  C m<sup>-2</sup>. Figure 10 also shows that the field re-

quired to transform the multidomain state to a rhombic phase depends on the number of domain walls in the system. However, the polarization components after the transition are the same for all the cases as eventually a single-domain rhombic state is established.

Figures 11(a), 11(b), and 11(c) show the evolution of average strain components  $\langle \eta_{xx}(E_{[11]}) \rangle - \langle \eta_{xx}(E_{[11]}=0) \rangle$ ,  $\langle \eta_{yy}(E_{[11]}) \rangle - \langle \eta_{yy}(E_{[11]}=0) \rangle$ , and  $\langle \eta_{xy}(E_{[11]}) \rangle - \langle \eta_{xy}(E_{[11]}=0) \rangle$ , respectively. The results of this figure can be understood in terms of the electric-field-induced symmetry changes. Let us first examine the results for the single-domain state. The zero-field initial state  $(0, 0.26)$  C m<sup>-2</sup> corresponds to a rectangular symmetry whereas the final state  $(0.21, 0.21)$  C m<sup>-2</sup> corresponds to a rhombic symmetry. This symmetry change is achieved by a uniaxial shrinkage along [01] and a uniaxial expansion along [10], as can be inferred from Figs. 11(a) and 11(b) (notice the sharp jump near the field induced transition). The behavior of shear strain [shown in Fig. 11(c)] is governed by the rotation undergone by the polarization vector. In contrast, the zero-field multidomain states correspond to a nearly square macroscopic symmetry due to the coexistence of two polarization (rectangular) vari-

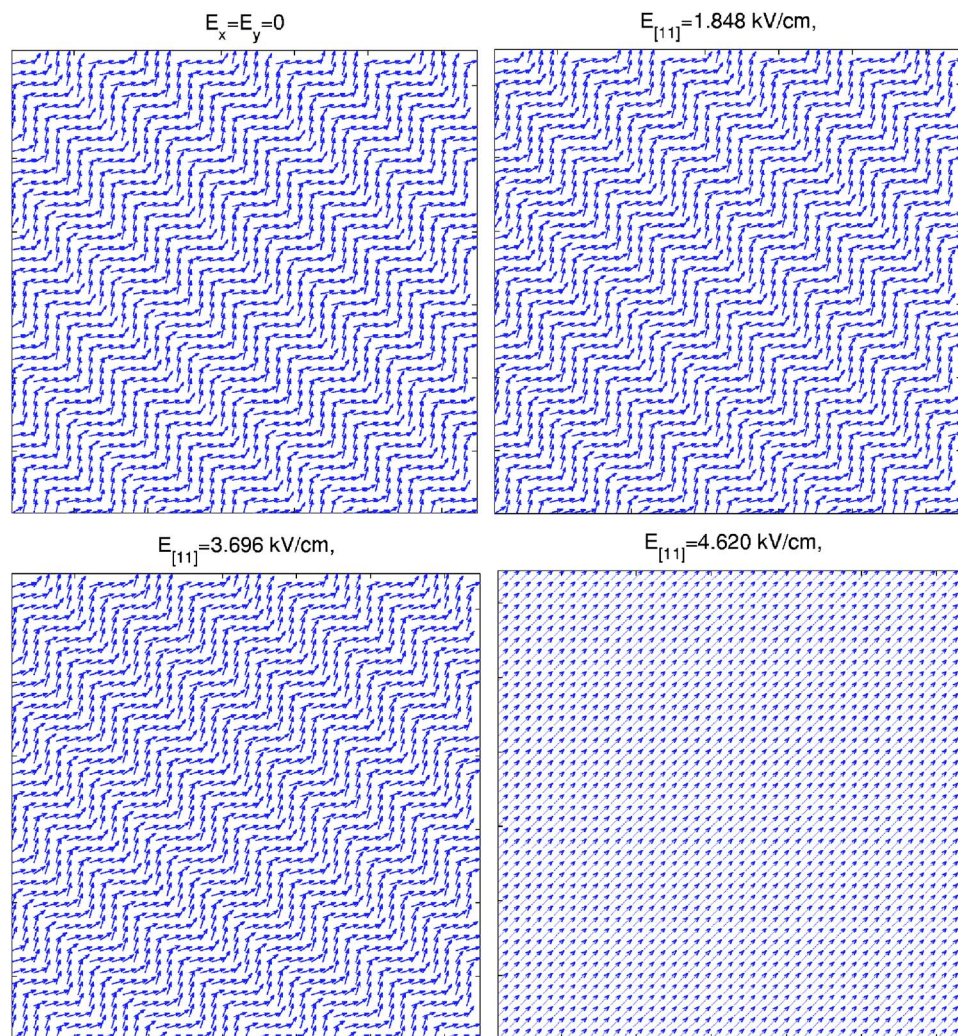


FIG. 9. (Color online) Evolution of domains for an electric field applied along the [11] direction to the multidomain state with domain size  $L_0 \sim 4.5$  nm. The corresponding electric field levels are indicated at the top of each snapshot.

ants. Hence, the multidomain evolutions of Figs. 7, 8, and 9 effectively correspond to electric-field-induced square to rhombic transitions. The jump due to the field-induced transition occurs at smaller electric field values as the domain size is decreased. The uniaxial strain the crystal undergoes after the transition is almost the same along the [10] and [01] directions. Interestingly, the saturation value of the strains is essentially the same for all the three multidomain evolutions. The magnitude of shear strains after the transition, on the other hand, depends on the domain size (or the number of domain walls) in the initial state. As seen in Fig. 11(c), the amount of shear experienced by the crystal is the largest for the case with  $L_0 \sim 22.6$  nm and the smallest for the  $L_0 \sim 4.5$  nm case. Preexisting shear strains at the domain walls limit the total shear experienced by the multidomain crystals, and thus the larger the number of domain walls in the initial state, the smaller the shear strains produced.

Figure 12 depicts the behavior of the longitudinal piezoelectric coefficients  $d_{33}^{[11]}$  for the three multidomain states as well as the analogous single-domain situation. The quantity  $d_{33}^{[11]}$  is calculated from the slope of the longitudinal strain

resolved along the [11] direction versus  $E_{[11]}$  curve. The resolved strain is calculated as  $\langle \eta_{[11]}(E_{[11]}) \rangle - \langle \eta_{[11]}(E_{[11]}=0) \rangle$ , where  $\eta_{[11]}$  is given by

$$\eta_{[11]} = \frac{1}{2}(\eta_{xx} + \eta_{yy} + \eta_{xy}). \quad (10)$$

It is clear that the low-field piezoelectric coefficients for the smallest domain size  $L_0 \sim 4.5$  nm are more enhanced compared to the domain patterns with  $L_0 \sim 22.6$  and 11.3 nm. The low-field piezoelectric coefficients for the coarser domain patterns are not much higher than the single-domain coefficients, consistent with recent experiments.<sup>17</sup> We believe that the enhancement is related to the response of unit cells in the domain wall regions as these regions become bigger with the domain size becoming smaller.

#### IV. SUMMARY AND DISCUSSIONS

We have used a Ginzburg-Landau formalism to study the domain-size dependence of the piezoelectric properties.

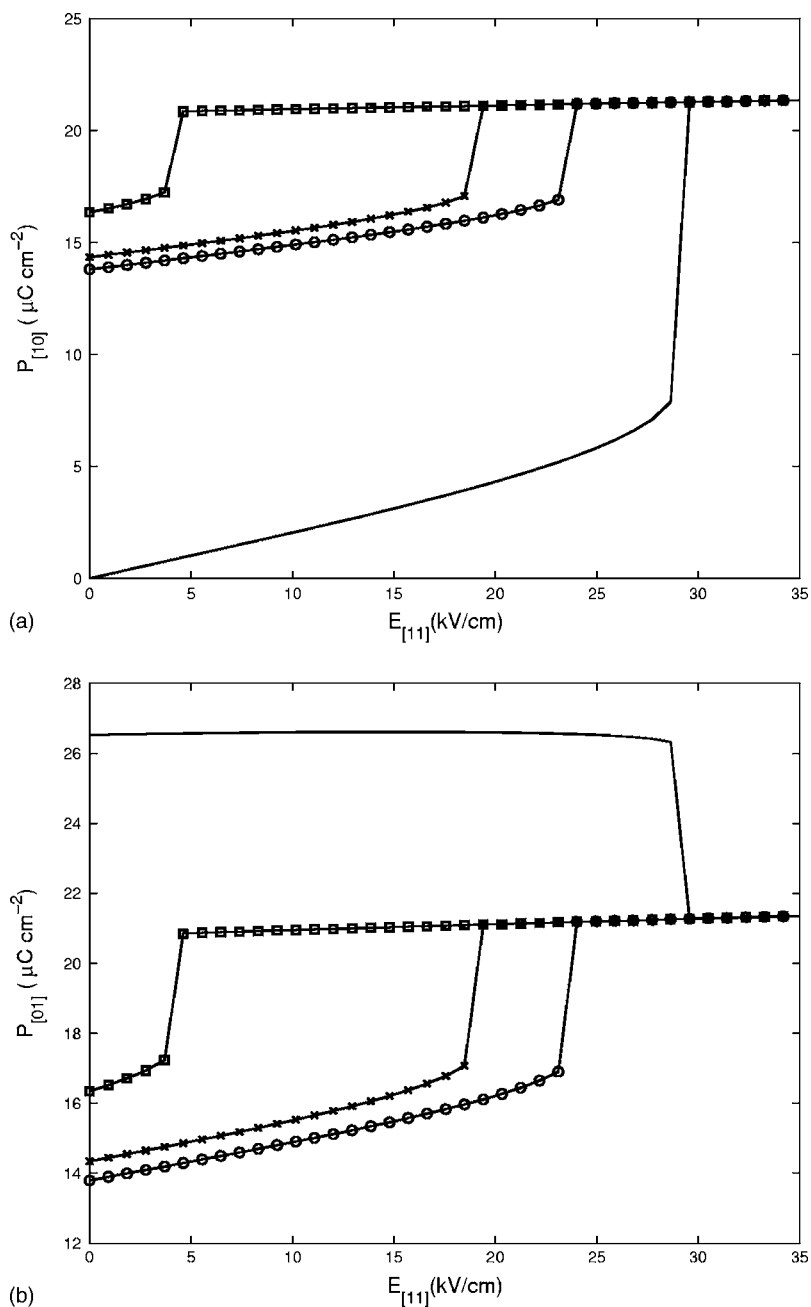


FIG. 10. Evolution of average polarizations  $P_{[10]}$  (a) and  $P_{[01]}$  (b) with the applied field  $E_{[11]}$ . The lines with circles correspond to the multidomain state of Fig. 7 (with domain size  $L_0 \sim 22.6$  nm), lines with crosses correspond to the multidomain state of Fig. 8 (with domain size  $L_0 \sim 11.3$  nm), and lines with squares correspond to the multidomain state of Fig. 9 (with domain size  $L_0 \sim 4.5$  nm). Solid lines correspond to the single-domain state.

The present work is inspired by the recent experiments of Wada and Tsurumi<sup>6</sup> on domain-engineered BaTiO<sub>3</sub> single crystals where the effect of the size of non-180° domains on the piezoelectric constants was studied. In our model calculation, we solved the 2D time-dependent-Ginzburg-Landau equations<sup>10</sup> with biased initial conditions (the free-energy parameters for BaTiO<sub>3</sub> were chosen from Ref. 9) to create three different multidomain states with different domain widths.

Two different directions of the applied field were considered. In the first case, the multidomain states were subjected to an electric field along the [01] direction, which is one of the four polar directions. The multidomain states switched to single-domain states polarized along the [01] direction, with

the state having the largest number of domain walls switching at the lowest electric field. The multidomain state with the smallest domain size also exhibited the largest value of the longitudinal piezoelectric constant  $d_{33}^{[01]}$ . This enhancement of the piezoelectric coefficient as the domain size is decreased reflects the metastability of the multidomain states which can become easily switchable as the number of domain walls is increased. However, this enhancement of the piezoelectric constant may not be very useful in practical applications as the multidomain states are not stable over a large range of electric fields.

We also considered the case where an electric field along the [11] direction is applied to the same multidomain states. This situation is analogous to the experiments of Wada and

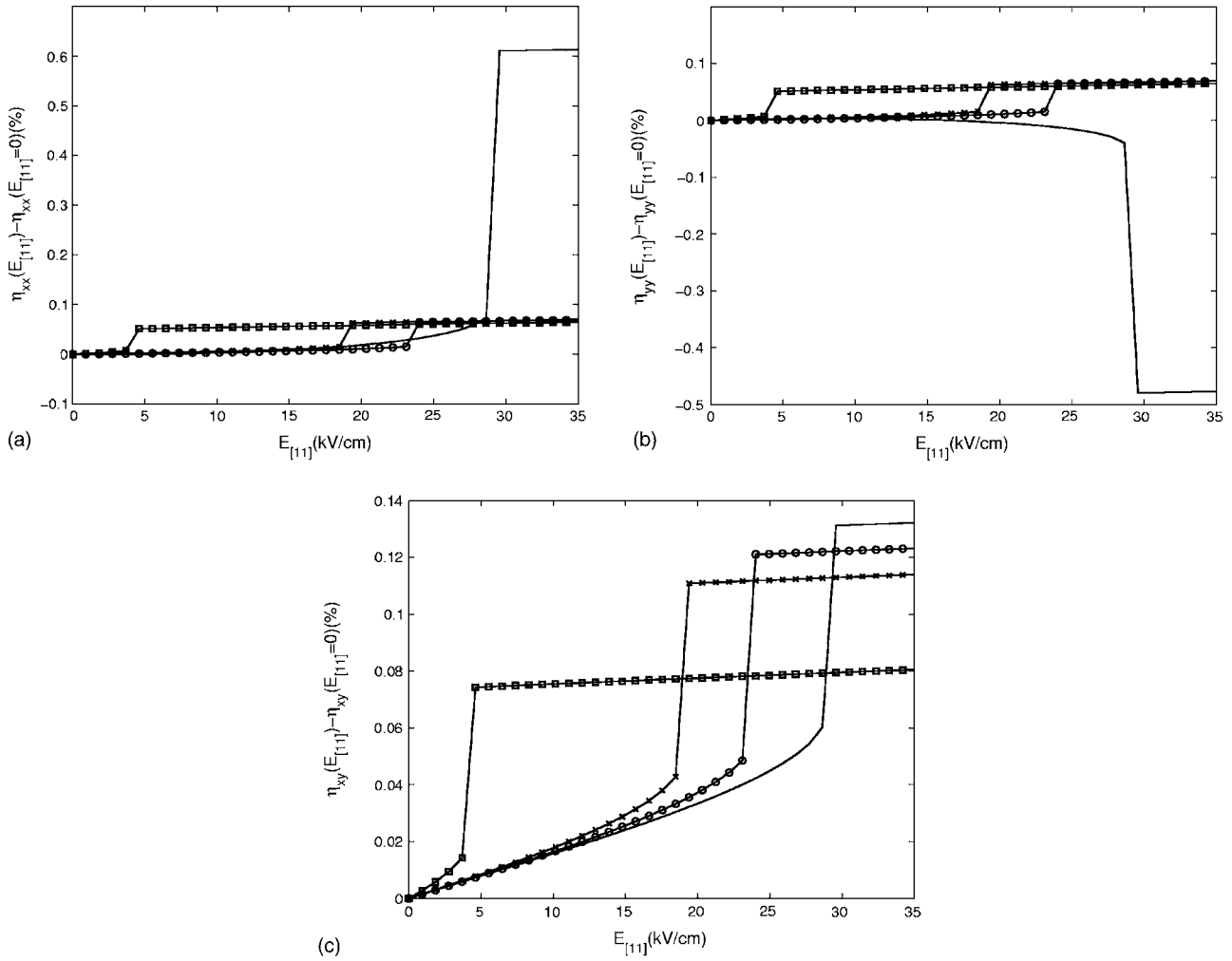


FIG. 11. Evolution of average strains  $\langle \eta_{xx}(E_{[11]}) \rangle - \langle \eta_{xx}(E_{[11]}=0) \rangle$  (a),  $\langle \eta_{yy}(E_{[11]}) \rangle - \langle \eta_{yy}(E_{[11]}=0) \rangle$  (b), and  $\langle \eta_{xy}(E_{[11]}) \rangle - \langle \eta_{xy}(E_{[11]}=0) \rangle$  (c) with the applied field  $E_{[11]}$ . The lines with circles correspond to the multidomain state of Fig. 7 (with domain size  $L_0 \sim 22.6$  nm), lines with crosses correspond to the multidomain state of Fig. 8 (with domain size  $L_0 \sim 11.3$  nm), and lines with squares correspond to the multidomain state of Fig. 9 (with domain size  $L_0 \sim 4.5$  nm). Solid lines correspond to the single-domain state.

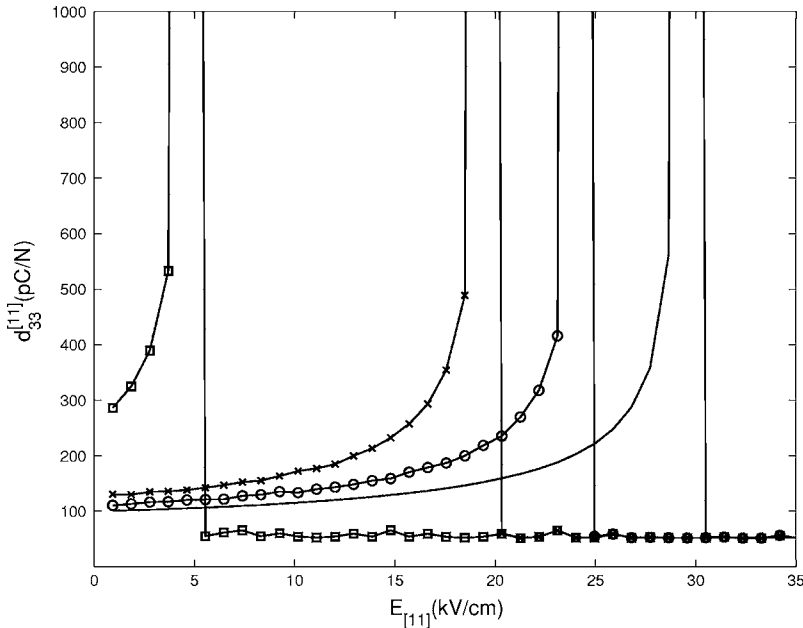


FIG. 12. Variation of  $d_{33}^{[11]}$  (the longitudinal piezoelectric constant along  $[11]$ ) with  $E_{[11]}$ . The lines with circles correspond to the multidomain state of Fig. 7 (with domain size  $L_0 \sim 22.6$  nm), lines with crosses correspond to the multidomain state of Fig. 8 (with domain size  $L_0 \sim 11.3$  nm), and lines with squares correspond to the multidomain state of Fig. 9 (with domain size  $L_0 \sim 4.5$  nm). Solid lines correspond to the single-domain state.

Tsurumi<sup>6</sup> who studied the piezoelectric properties of tetragonal domain-engineered BaTiO<sub>3</sub> single crystals under an electric field along [111]. For this case, we found that the multidomain states remain stable until a field-induced rectangular to rhombic transition takes place. Interestingly, we found that the transition occurs at smaller fields as the domain size is decreased. Since proximity to the field-induced transition enhances the piezoelectric constants, the low-field piezoelectric constant for the smallest size simulated by us is found to be significantly higher than that for the single crystal and multidomains with bigger domain sizes. Thus, the

role of the domain walls in nucleating a field-induced transition may be the cause of the enhanced piezoelectricity in small-sized engineered domains observed by Wada and Tsurumi.<sup>6</sup> This enhancement may be used in practical applications, provided the field is not too close to the field-induced transition.

#### ACKNOWLEDGMENT

This work was supported by the U.S. Department of Energy and NSF Grant No. DGE-9987589.

- 
- <sup>1</sup>M. E. Lines and A. M. Glass, *Principles and Applications of Ferroelectrics and Related Materials* (Clarendon, Oxford, 1979).
- <sup>2</sup>K. Uchino, *Piezoelectric Actuators and Ultrasonic Motors* (Kluwer Academic, Boston, 1996).
- <sup>3</sup>S. E. Park and T. R. Shrout, *J. Appl. Phys.* **82**, 1804 (1997).
- <sup>4</sup>S. Wada, S. Suzuki, T. Noma, T. Suzuki, M. Osada, M. Kakihana, S. E. Park, L. E. Cross, and T. R. Shrout, *Jpn. J. Appl. Phys., Part 1* **38**, 5505 (1999).
- <sup>5</sup>H. Fu and R. E. Cohen, *Nature (London)* **403**, 281 (2000).
- <sup>6</sup>S. Wada and T. Tsurumi, *Br. Ceram. Trans.* **103**, 93 (2004).
- <sup>7</sup>A. Garcia and D. Vanderbilt, *Appl. Phys. Lett.* **72**, 2981 (1998).
- <sup>8</sup>N. Sai, K. M. Rabe, and D. Vanderbilt, *Phys. Rev. B* **66**, 104108 (2002).
- <sup>9</sup>A. J. Bell, *J. Appl. Phys.* **89**, 3907 (2001).
- <sup>10</sup>R. Ahluwalia, T. Lookman, A. Saxena, and W. Cao, *Appl. Phys. Lett.* **84**, 3450 (2004).
- <sup>11</sup>S. Nambu and D. A. Sagala, *Phys. Rev. B* **50**, 5838 (1994).
- <sup>12</sup>H. L. Hu and L. Q. Chen, *Mater. Sci. Eng., A* **238**, 182 (1997).
- <sup>13</sup>R. Ahluwalia and W. Cao, *Phys. Rev. B* **63**, 012103 (2001).
- <sup>14</sup>E. A. H. Love, *A Treatise on the Mathematical Theory of Elasticity* (Dover, New York, 1944).
- <sup>15</sup>A. M. Bratkovsky and A. P. Levanyuk, in *Fundamental Physics of Ferroelectrics*, edited by R. E. Cohen, AIP Conf. Proc. No. 626 (AIP, Melville, NY, 2002), p. 252.
- <sup>16</sup>T. Mitsui, I. Tatsuzaki, and E. Nakamura, *An Introduction to the Physics of Ferroelectrics* (Gordon and Breach, New York, 1974).
- <sup>17</sup>D. Damjanovic, M. Budimir, M. Davis, and N. Setter, *Appl. Phys. Lett.* **83**, 527 (2003).